




Cite this: *Chem. Sci.*, 2020, 11, 2093 All publication charges for this article have been paid for by the Royal Society of Chemistry

# A possible unaccounted source of atmospheric sulfate formation: amine-promoted hydrolysis and non-radical oxidation of sulfur dioxide†

Shixian Wang,<sup>a</sup> Xiao Cheng Zeng, <sup>\*ba</sup> Hui Li  <sup>\*a</sup> and Joseph S. Francisco  <sup>\*c</sup>

Numerous field and laboratory studies have shown that amines, especially dimethylamine (DMA), are crucial to atmospheric particulate nucleation. However, the molecular mechanism by which amines lead to atmospheric particulate formation is still not fully understood. Herein, we show that DMA molecules can also promote the conversion of atmospheric SO<sub>2</sub> to sulfate. Based on *ab initio* simulations, we find that in the presence of DMA, the originally endothermic and kinetically unfavourable hydrolysis reaction between gaseous SO<sub>2</sub> and water vapour can become both exothermic and kinetically favourable. The resulting product, bisulfite NH<sub>2</sub>(CH<sub>3</sub>)<sub>2</sub><sup>+</sup>·HSO<sub>3</sub><sup>-</sup>, can be readily oxidized by ozone under ambient conditions. Kinetic analysis suggests that the hydrolysis rate of SO<sub>2</sub> and DMA with water vapour becomes highly competitive with and comparable to the rate of the reaction between SO<sub>2</sub> and OH•, especially under the conditions of heavily polluted air and high humidity. We also find that the oxidants NO<sub>2</sub> and N<sub>2</sub>O<sub>5</sub> (whose role in sulfate formation is still under debate) appear to play a much less significant role than ozone in the aqueous oxidation reaction of SO<sub>2</sub>. The newly identified oxidation mechanism of SO<sub>2</sub> promoted by both DMA and O<sub>3</sub> provides another important new source of sulfate formation in the atmosphere.

Received 20th September 2019

Accepted 9th January 2020

DOI: 10.1039/c9sc04756e

rsc.li/chemical-science

## 1 Introduction

Sulfuric acid in the atmosphere, mainly produced by the oxidation of gaseous sulfur dioxide, is known as the most important nucleating agent in the earliest stage of atmospheric new particle formation (NPF), as it possesses the lowest vapour pressure (<0.001 mmHg at 298 K) among the gaseous species in the atmosphere.<sup>1–9</sup> SO<sub>2</sub> in the atmosphere is mainly oxidized by OH• radicals produced from excited oxygen and water vapour.<sup>10–12</sup> However, numerous observations indicate that there is insufficient OH• to account for the unexpectedly rapid growth in H<sub>2</sub>SO<sub>4</sub> concentration in the highly polluted atmosphere, in which the high aerosol concentration can actually block solar ultraviolet radiation and lower the concentration of OH• radicals, thereby preventing them from participating in photochemical reactions.<sup>5</sup> Moreover, OH• oxidation alone cannot explain the observed level of H<sub>2</sub>SO<sub>4</sub> at nighttime.<sup>13</sup>

On the other hand, although the abundance of the common oxidizing gases O<sub>3</sub> and NO<sub>x</sub> is much higher than that of OH• radicals in the atmosphere, previous *ab initio* calculations show that the direct oxidation of SO<sub>2</sub> by O<sub>3</sub>/NO<sub>x</sub> in the gas phase is kinetically unfeasible due to extremely high activation barriers. The hydrolysis of gaseous SO<sub>2</sub> is proposed as an alternative reaction pathway to yield H<sub>2</sub>SO<sub>4</sub> because sulfurous acid can be more easily oxidized to sulfuric acid by some moderate oxidants, *e.g.*, ozone and NO<sub>x</sub>.<sup>14–17</sup> However, the hydrolysis of SO<sub>2</sub> in the gas phase has also been shown to be both thermodynamically and kinetically unfavourable *via* high-level quantum mechanical (QM) calculations<sup>10,18–20</sup> since the hydrolysis of SO<sub>2</sub> with either H<sub>2</sub>O monomer or dimer is an endothermic process and, again, entails very high energy barriers.<sup>10</sup> Hence, new oxidation pathways must be explored to explain the fast conversion of SO<sub>2</sub> to atmospheric H<sub>2</sub>SO<sub>4</sub>.

Atmospheric bases, such as ammonia (NH<sub>3</sub>), are another important contributor to initial sulfate aerosols.<sup>21</sup> In addition, both cloud chamber studies and field measurements have revealed that atmospheric amines, especially dimethylamine (DMA), also play a surprisingly crucial role in the NPF process, even though their concentrations are two or three orders of magnitude lower than that of NH<sub>3</sub>.<sup>22–30</sup> For example, Almeida *et al.* detected that a 5 pptv level of DMA can enhance the particle formation rate more than 1000-fold than 250 pptv NH<sub>3</sub>.<sup>8</sup> More recently, Yao *et al.* reported that H<sub>2</sub>SO<sub>4</sub>·DMA·H<sub>2</sub>O nucleation leads to high NPF rates in urban areas of China.<sup>30</sup> Li

<sup>a</sup>Beijing Advanced Innovation Center for Soft Matter Science and Engineering, Beijing University of Chemistry Technology, Beijing 10029, China. E-mail: hli@mail.buct.edu.cn

<sup>b</sup>Department of Chemistry, University of Nebraska-Lincoln, Lincoln, Nebraska, USA 68588. E-mail: xzeng1@unl.edu

<sup>c</sup>Department of Earth and Environmental Sciences, University of Pennsylvania, Philadelphia, Pennsylvania, USA 19104. E-mail: frjoseph@sas.upenn.edu

† Electronic supplementary information (ESI) available. See DOI: 10.1039/c9sc04756e



*et al.* found that sulfamic acid, produced from  $\text{SO}_3$  and high concentrations of  $\text{NH}_3$ , can directly participate in  $\text{H}_2\text{SO}_4 \cdot \text{DMA}$  clustering.<sup>31</sup> Currently, it is widely accepted that DMA, similar to  $\text{NH}_3$ , can further stabilize sulfate clusters through salification with  $\text{H}_2\text{SO}_4$ . On the other hand, although Liu *et al.* showed that alkaline gases, such as ammonia, can promote the hydrolysis of  $\text{SO}_2$  to form  $\text{H}_2\text{SO}_3$  (ref. 22) and Chen *et al.* proposed that alkaline aerosols can trap  $\text{SO}_2$ , then being oxidized by  $\text{NO}_2$ ,<sup>14</sup> the role played by DMA molecules in atmospheric chemistry is still incompletely understood, despite its fundamental importance for exploring the role of amines in atmospheric chemistry.

Here, we show that atmospheric amines can play a key role in the formation of sulfates at high relative humidity (RH) and low illumination, thereby contributing to enhanced aerosol formation on highly polluted days. *Ab initio* simulations demonstrate that the presence of methylamine (MA)/DMA molecules leads to exothermic hydrolysis of  $\text{SO}_2$  with water vapour, without a barrier, to a product that can be oxidized by  $\text{O}_3$  and  $\text{NO}_x$ .  $\text{O}_3$  is also found to be a stronger oxidant than  $\text{NO}_x$  in the amine-assisted oxidation of  $\text{SO}_2$ . As a result, the concentration level of atmospheric  $\text{H}_2\text{SO}_4$  from aqueous oxidation may be mainly controlled by the concentration of  $\text{O}_3$  rather than that of  $\text{NO}_x$ . Based on transition state theory (TST) analysis and the observed concentrations of the participating atmospheric species, the rate of the  $\text{SO}_2$  hydrolysis reaction with the assistance of DMA at 100% RH is even higher than the rate of  $\text{SO}_2$  oxidation by  $\text{OH}\cdot$ . This finding may shed new light on the long-standing

endeavour to identify the unknown oxidation pathway leading to atmospheric sulfate formation.

## 2 Results and discussion

### 2.1 Hydrolysis of $\text{SO}_2$ assisted by DMA

The potential energy surfaces (PESs) for the hydrolysis reaction of  $\text{SO}_2$ , MA/DMA and  $n\text{H}_2\text{O}$  ( $n = 1-3$ ) are shown in Fig. 1(a-b) and S1 in ESI.† In the reaction with the water monomer (Fig. 1(a)), the breaking of the O-H bond of water in the presence of MA and DMA requires activation energies of 5.8 and 3.2 kcal mol<sup>-1</sup>, respectively, indicating that both reactions can take place quite readily under ambient conditions. In contrast, the process of  $\text{SO}_2 + \text{H}_2\text{O} \rightarrow \text{H}_2\text{SO}_3$  in the gas phase needs to overcome a high energy barrier of 33.9 kcal mol<sup>-1</sup>.<sup>12</sup> Note that previous quantum-mechanical (QM) calculations showed that atmospheric ammonia can also lower the barrier for the hydrolysis of  $\text{SO}_2$  to ~12.0 kcal mol<sup>-1</sup>.<sup>22</sup> However, this energy barrier is still quite high for a reaction to take place at room temperature. According to our calculations, the hydrolysis barriers with MA and DMA are approximately 6.0 and 9.0 kcal mol<sup>-1</sup> lower than the barrier with  $\text{NH}_3$ , respectively, suggesting that amines can promote  $\text{SO}_2$  hydrolysis more strongly than  $\text{NH}_3$ . Furthermore, spontaneous ionization to form  $\text{HSO}_3^-$  and  $\text{NH}_3\text{CH}_3^+/\text{NH}_2(\text{CH}_3)_2^+$  during the hydrolysis reactions is also observed.

The energy barrier for hydrolysis can be further lowered by introducing an additional water molecule to the reaction through

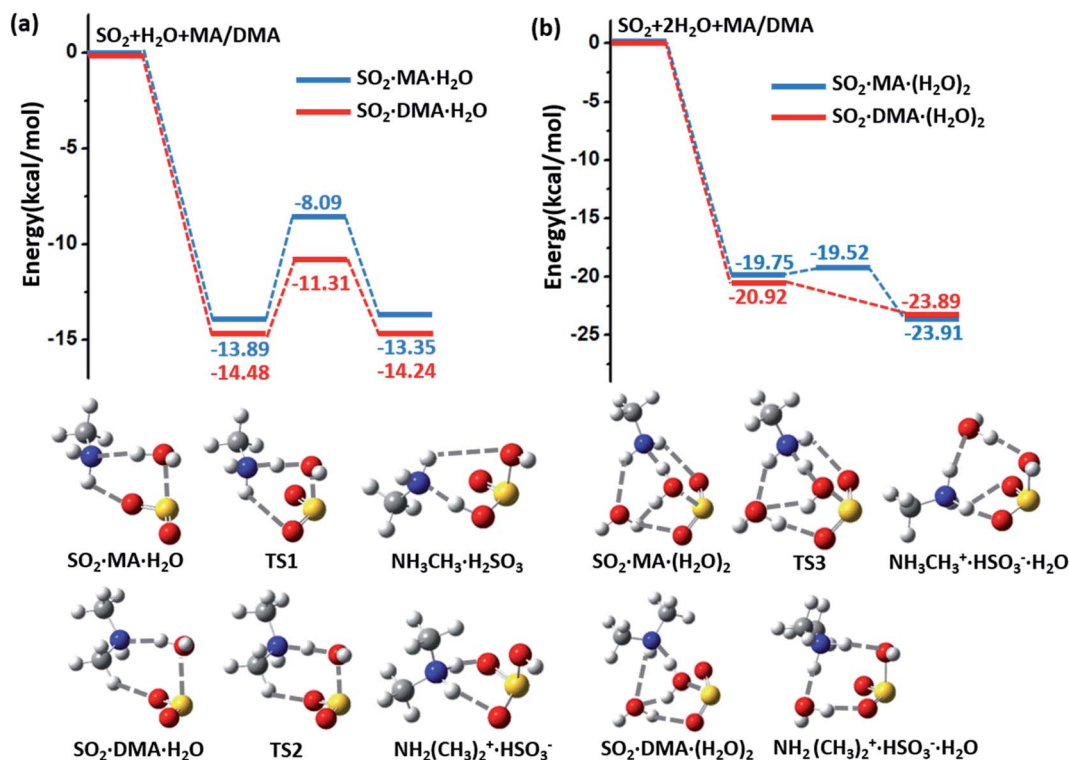


Fig. 1 (a) Potential energy profiles for the hydrolysis reactions of MA (blue lines)/DMA (red lines),  $\text{SO}_2$ , and  $\text{H}_2\text{O}$  monomer. (b) Potential energy profiles for the hydrolysis reactions of MA (blue lines)/DMA (red lines),  $\text{SO}_2$ , and  $\text{H}_2\text{O}$  dimer. The energy profiles are calculated at the M06-2X/cc-pVDZ-F12 level with zero-point-energy (ZPE) correction.



the formation of a ring structure in the transition state, as shown in Fig. 1(b). The hydrolysis of  $\text{SO}_2$  with a water dimer and DMA can become barrierless. Likewise, hydrolysis with  $(\text{H}_2\text{O})_n$  ( $n \geq 3$ ) are also barrierless reactions (ESI Fig. S1†). In addition, increasing the number of water and DMA molecules also promotes further ionization of the already formed  $\text{H}_2\text{SO}_3$  and amine molecules. As shown in ESI Fig. S2†(a),  $\text{H}_2\text{SO}_3$  is partially ionized to  $\text{HSO}_3^-$  in the  $(\text{DMA})_2 \cdot \text{H}_2\text{SO}_3 \cdot (\text{H}_2\text{O})_n$  ( $n = 1-3$ ) clusters, while complete ionization of  $\text{H}_2\text{SO}_3$  and DMA to  $(\text{NH}_2(\text{CH}_3)_2)_2 \cdot \text{SO}_3^{2-}$  is observed in the presence of  $(\text{H}_2\text{O})_n$  ( $n \geq 4$ ) with a very low dissociation barrier of  $0.24 \text{ kcal mol}^{-1}$  (ESI Fig. S2(b)†). Next, we show that the complete ionization of  $\text{H}_2\text{SO}_3$  can benefit its oxidation, a phenomenon that may occur on aerosol surfaces (with high pH) in air with high concentrations of DMA and water.

The spontaneous formation and ionization processes of bisulfite/sulfite are confirmed by Born–Oppenheimer molecular dynamics (BOMD) simulation (Fig. 2). As shown by the BOMD trajectories at 300 K in Fig. 2(a), the hydrolysis of  $\text{SO}_2$  with a water dimer and MA molecule is a very fast process, where the OH bond of a bridging water molecule breaks during the initial 0.33 ps of the BOMD simulation. Meanwhile, the N–H and O–S bond distances decrease to  $\sim 1.07$  and  $\sim 1.78 \text{ \AA}$ , respectively, suggesting the formation of  $\text{NH}_3\text{CH}_3^+ \cdot \text{HSO}_3^- \cdot \text{H}_2\text{O}$ . It is observed that the system does not maintain the ionized form and returns back to the molecular state of  $\text{SO}_2$  after 2.70 ps, indicating the reversible transition between  $\text{SO}_2$  and  $\text{HSO}_3^-$  due to the thermal effect. It is interesting that such a chemical equilibrium can be sensitively regulated by temperature. The simulation system maintains the form of  $\text{NH}_3\text{CH}_3^+ \cdot \text{HSO}_3^-$  at 300 K for  $\sim 2.4$  ps during the total BOMD simulation time of 20 ps (lower panel in Fig. 2(b)), while the time period that  $\text{NH}_3\text{CH}_3^+ \cdot \text{HSO}_3^-$  lasts is approximately six times longer at 250 K ( $\sim 12.2$  ps) than at 300 K (upper panel in Fig. 2(b)). The BOMD simulation of  $\text{SO}_2 \cdot \text{DMA} \cdot (\text{H}_2\text{O})_2$  shows a similar trajectory as

that of the  $\text{SO}_2 \cdot \text{MA} \cdot (\text{H}_2\text{O})_2$  system (Fig. 2(c) and (d)), where the time periods of the  $\text{NH}_2(\text{CH}_3)_2^+ \cdot \text{HSO}_3^-$  state are 9.1 and 10.6 ps at 300 and 250 K, respectively. Clearly, lower temperature is beneficial for bisulfite/sulfite formation due to its entropy being lower than that of the loose  $\text{SO}_2 \cdot \text{H}_2\text{O}$  cluster.

Previous studies have suggested that heterogeneous reactions on the surface of water droplets play crucial roles in atmospheric chemistry, such as the ionization of  $\text{N}_2\text{O}_4$ .<sup>32,33</sup> Zhong *et al.* found that  $\text{SO}_2$  on a water nanodroplet tends to have an S–O bond exposed to the air that can readily react with other gaseous species in the air.<sup>34</sup> Here, BOMD simulations also confirm that increasing the size of the water cluster can move the  $\text{SO}_2 \leftrightarrow \text{HSO}_3^-$  equilibrium towards the right-hand side. As shown in ESI Fig. S3(a) and (b),†  $\text{SO}_2$ , MA/DMA, and two water molecules quickly convert to  $\text{NH}_3\text{CH}_3^+/\text{NH}_2(\text{CH}_3)_2^+ \cdot \text{HSO}_3^- \cdot \text{H}_2\text{O}$  cyclic structures, which remain stable on the water cluster during the BOMD simulation at 300 K. By contrast, no similar structure is formed from  $\text{SO}_2$  and  $\text{NH}_3$  during the BOMD simulation (ESI Fig. S3(c)†), implying that the amines have a unique promotion effect on the hydrolysis of  $\text{SO}_2$ . The  $\text{NH}_2(\text{CH}_3)_2^+ \cdot \text{HSO}_3^-$  complex on the water droplet can also uptake an additional DMA molecule to form  $(\text{NH}_2(\text{CH}_3)_2^+)_2 \cdot \text{SO}_3^{2-}$ , as shown in ESI Fig. S3(d).†

## 2.2 Oxidation of $\text{NH}_2(\text{CH}_3)_2^+ \cdot \text{HSO}_3^-$ and $(\text{NH}_2(\text{CH}_3)_2^+)_2 \cdot \text{SO}_3^{2-}$ by $\text{O}_3$

The oxidation process of  $\text{NH}_2(\text{CH}_3)_2^+ \cdot \text{HSO}_3^-$  by  $\text{O}_3$  is divided into two steps: (1) Adsorption of  $\text{O}_3$  and (2) dissociation of  $[\text{SO}_3 \cdot \text{O}_3\text{H}]^-$ , as shown in the energy profiles in Fig. 3(a) and (b). The oxidation starts from the physical adsorption of  $\text{O}_3$  with one oxygen atom approaching the  $\text{HSO}_3^-$  group ( $E_{\text{ads}} = -3.03 \text{ kcal mol}^{-1}$ ), and then the  $\text{O}_3$  molecule is chemically adsorbed to  $\text{HSO}_3^-$  by forming a cyclic structure,  $\text{NH}_2(\text{CH}_3)_2^+$ .

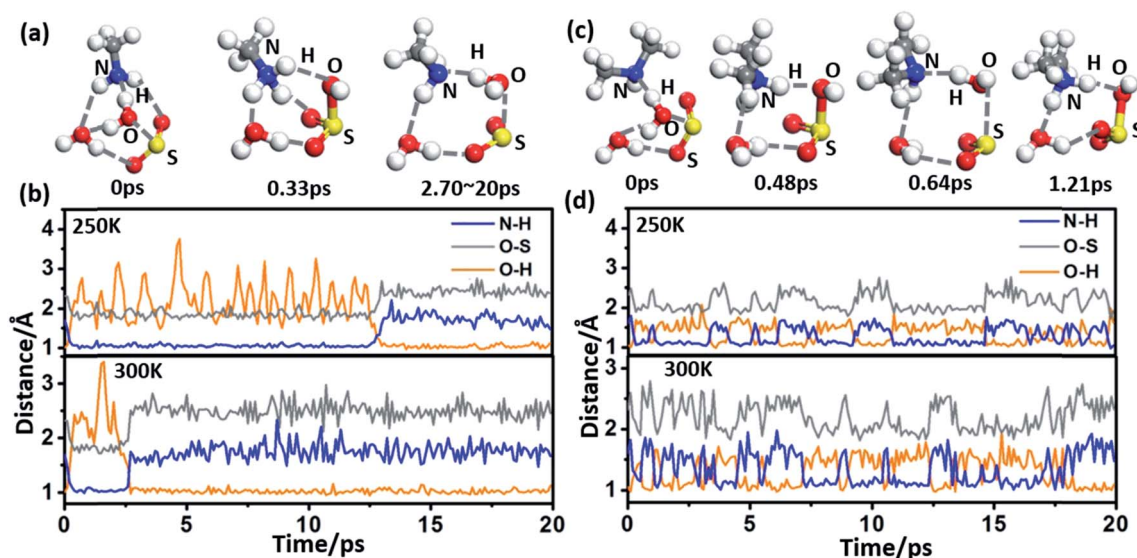


Fig. 2 (a) Snapshots taken from the BOMD simulation of  $\text{SO}_2 \cdot \text{MA} \cdot (\text{H}_2\text{O})_2$  at 300 K. (b) Time evolution of the O–H, O–S, and N–H bond lengths in  $\text{SO}_2 \cdot \text{MA} \cdot (\text{H}_2\text{O})_2$  at 250 and 300 K. (c) Snapshots taken from the BOMD simulation of  $\text{SO}_2 \cdot \text{DMA} \cdot (\text{H}_2\text{O})_2$  at 300 K. (d) Time evolution of the O–H, O–S, and N–H bond lengths in  $\text{SO}_2 \cdot \text{DMA} \cdot (\text{H}_2\text{O})_2$  at 250 and 300 K, respectively.



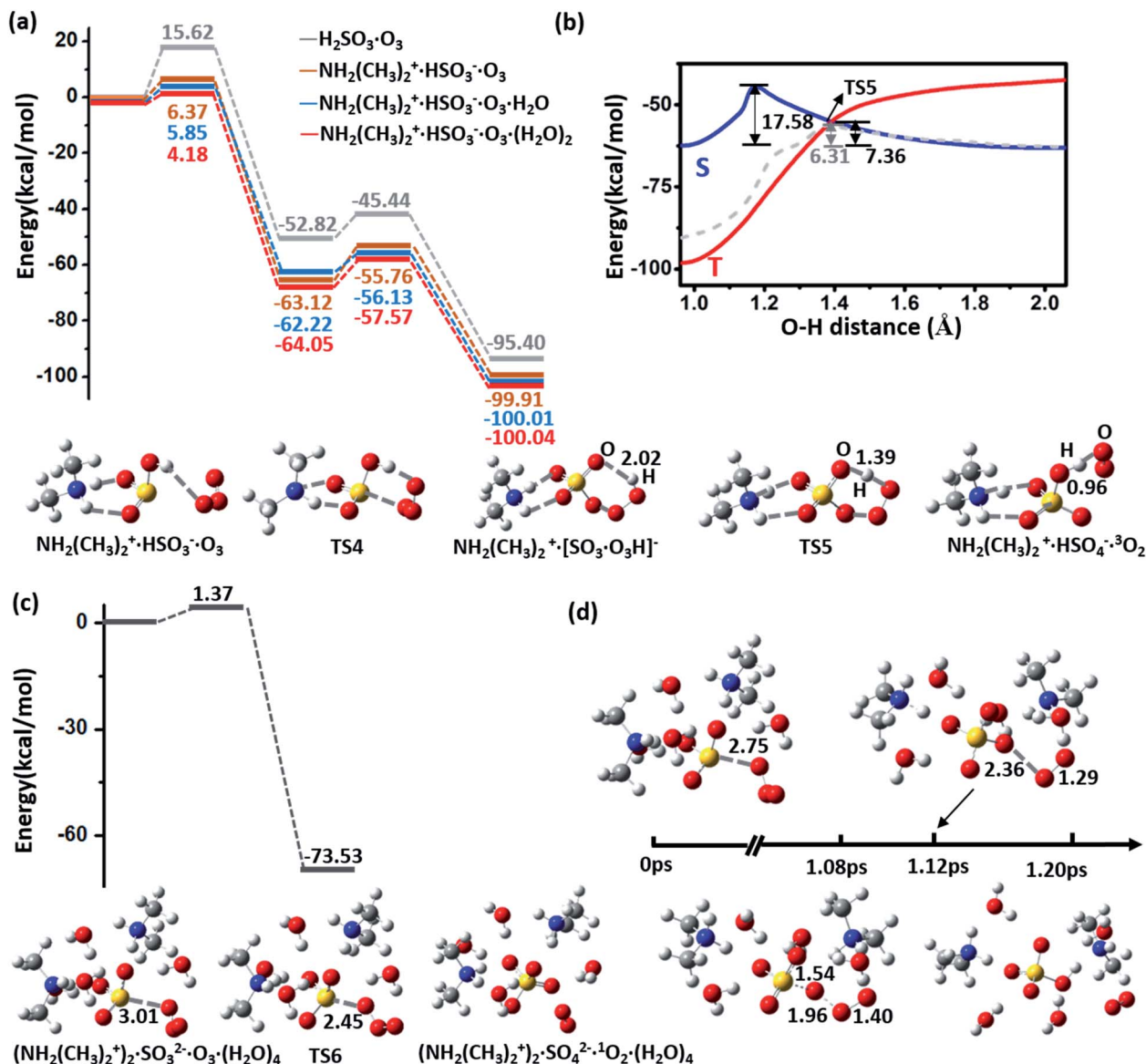


Fig. 3 (a) Potential energy profiles for the oxidation reactions of  $\text{H}_2\text{SO}_3/\text{CH}_2(\text{CH}_3)_2^+\cdot\text{HSO}_3^-\cdot(\text{H}_2\text{O})_n$  ( $n = 0, 1, 2$ ) and  $\text{O}_3$ . Snapshots are taken from the BOMD simulation. (b) Potential energy versus the O-H distance in  $\text{CH}_2(\text{CH}_3)_2^+\cdot[\text{SO}_3\cdot\text{O}_3\text{H}]^-$ . The blue and red lines correspond to the singlet and triplet multiplicities, respectively. The grey line is obtained from the spin-polarized calculation with the PBE functional in the VASP. Snapshots are taken from the BOMD simulation. (c) Potential energy profiles for the oxidation reactions of  $(\text{CH}_2(\text{CH}_3)_2^+)_2\cdot\text{SO}_3^{2-}\cdot(\text{H}_2\text{O})_4$  and  $\text{O}_3$ . Snapshots are taken from the BOMD simulation. (d) Snapshots are taken from the BOMD simulation of  $(\text{CH}_2(\text{CH}_3)_2^+)_2\cdot\text{SO}_3^{2-}\cdot\text{O}_3\cdot(\text{H}_2\text{O})_4$  at 300 K. All energy profiles are calculated at the M06-2X/cc-pVDZ-F12 level with ZPE correction.

$[\text{SO}_3\cdot\text{O}_3\text{H}]^-$ , as an intermediate state. This process is highly exothermic ( $\Delta E = -63.12 \text{ kcal mol}^{-1}$ ) and overcomes a low barrier of  $6.37 \text{ kcal mol}^{-1}$ , which is  $9.25 \text{ kcal mol}^{-1}$  lower than the energy barrier without an amine (Fig. 3(a)). This energy barrier can be further lowered by adsorption of additional water molecules, where the energy barrier equals  $5.85$  and  $4.18 \text{ kcal mol}^{-1}$  for one and two  $\text{H}_2\text{O}$  molecules, respectively (Fig. 3(a)). Due to the low energy barrier, formation of the  $\text{NH}_2(\text{CH}_3)_2^+\cdot[\text{SO}_3\cdot\text{O}_3\text{H}]^-$  complex can spontaneously occur during the BOMD simulation at room temperature (ESI Fig. S4†).

As  $\text{NH}_2(\text{CH}_3)_2^+\cdot[\text{SO}_3\cdot\text{O}_3\text{H}]^-$  is an extremely stable intermediate state, the dissociation of  $[\text{SO}_3\cdot\text{O}_3\text{H}]^-$  needs to overcome a relatively high energy barrier ( $E_a = 17.58 \text{ kcal mol}^{-1}$ ) to

produce  $\text{HSO}_4^-$  and singlet  $\text{O}_2$  in the spin-restricted calculation (Fig. 3(b)). This barrier seems too high for a room-temperature reaction to occur. However, it is known that unstable singlet  $\text{O}_2$  in the atmosphere can quickly convert to the triplet ground state<sup>35</sup> through collision and that, in particular, the strong spin-orbit interaction of the heavy element sulfur can greatly enhance the spin-flipping rate. Thus, the real dissociation process is accompanied by a spin-flipping process, which can greatly lower the dissociation barrier. Because the O-H stretching vibration corresponds to the main imaginary frequency of the transition state, we scan the energy surface versus the O-H distance ( $d_{\text{OH}}$ ) of  $[\text{SO}_3\cdot\text{O}_3\text{H}]^-$ , as shown in Fig. 3(b). The cross-point ( $d_{\text{OH}} = 1.39 \text{ \AA}$ ) between the singlet and



triplet Born–Oppenheimer potential surfaces is found to yield a dissociation barrier of  $7.36 \text{ kcal mol}^{-1}$ , indicating the kinetic feasibility of the oxidation process under ambient conditions. The low dissociation barrier ( $E_a = 6.31 \text{ kcal mol}^{-1}$ ) is also confirmed by a calculation at the spin-polarized Perdew–Burke–Ernzerhof (PBE)/plane-wave level,<sup>36</sup> as implemented in the Vienna *Ab initio* Simulation Package (VASP 5.3).<sup>37</sup> The dissociation reaction is also highly exothermic ( $\Delta E = -36.79 \text{ kcal mol}^{-1}$ ). Unlike the barrier to the adsorption of  $\text{O}_3$ , the dissociation barrier is minimally affected by additional vicinal water molecules (Fig. 3(a) and ESI Fig. S5†).

Moreover, the dissociation of  $\text{HSO}_3^-$  to  $\text{SO}_3^{2-}$ , which generally happens on alkaline aerosol surface, can promote oxidation with  $\text{O}_3$ . A cluster containing one  $\text{H}_2\text{SO}_3$ , two DMA, and four  $\text{H}_2\text{O}$  molecules is chosen to mimic this situation, where the DMA and  $\text{H}_2\text{SO}_3$  molecules spontaneously form  $\text{NH}_2(\text{CH}_3)_2^+$  and  $\text{SO}_3^{2-}$ . As shown in Fig. 3(c), the oxidation becomes a one-step reaction with an extremely low barrier ( $E_a = 1.37 \text{ kcal mol}^{-1}$ ). This oxidation process can be reproduced in the BOMD simulation as well (Fig. 3(d)).

### 2.3 Oxidation of $\text{NH}_2(\text{CH}_3)_2^+ \cdot \text{HSO}_3^-$ with $\text{NO}_x$

$\text{NH}_2(\text{CH}_3)_2^+ \cdot \text{HSO}_3^-$  can be oxidized by  $\text{NO}_2$  to form the radical  $\text{NH}_2(\text{CH}_3)_2^+ \cdot \text{SO}_3^-$  and  $\text{HNO}_2$  (HONO) with an energy barrier of

$13.08 \text{ kcal mol}^{-1}$  and a potential energy change of  $-5.15 \text{ kcal mol}^{-1}$ , as shown by the energy profiles and corresponding structures displayed in ESI Fig. 4(a) and S6(a),† respectively. In contrast to this oxidation reaction, the oxidation process without DMA has a relatively higher barrier ( $18.02 \text{ kcal mol}^{-1}$ ) and a positive energy change ( $6.30 \text{ kcal mol}^{-1}$ ), as shown in Fig. 4(a). Similar to the barrier for  $\text{O}_3$  oxidation, the barrier for oxidizing  $\text{NH}_2(\text{CH}_3)_2^+ \cdot \text{SO}_3^-$  with  $\text{NO}_2$  can be lowered by extra neighbouring water molecules; *e.g.*, the values of the oxidation barrier in the presence of the water monomer and dimer are equal to  $10.20$  and  $8.32 \text{ kcal mol}^{-1}$ , respectively. Such a barrier is believed to be even lower on the surface of aqueous aerosols.

The  $\text{NH}_2(\text{CH}_3)_2^+ \cdot \text{SO}_3^-$  radical product is an active radical, so it can easily react with other radicals, such as  $\text{O}_2$ ,  $\text{NO}_2$ , and  $\text{OH}^\cdot$ . For example, our calculations demonstrate that  $\text{NH}_2(\text{CH}_3)_2^+ \cdot \text{SO}_3^- \cdot (\text{H}_2\text{O})_n$  ( $n \geq 1$ ) and another  $\text{NO}_2$  molecule can spontaneously form a  $\text{NH}_2(\text{CH}_3)_2^+ \cdot \text{HSO}_4^- \cdot (\text{H}_2\text{O})_{n-1}$  cluster (ESI Fig. S6(b)†). In addition,  $\text{HNO}_2$ , the other product of this oxidation reaction, is also an important precursor of  $\text{OH}^\cdot$  radicals in the atmosphere.<sup>38,39</sup>

The potential energy profiles of  $\text{NH}_2(\text{CH}_3)_2^+ \cdot \text{HSO}_3^- \cdot (\text{H}_2\text{O})_n$  ( $n = 0-3$ ) oxidized by  $\text{N}_2\text{O}_5$ , another abundant oxidative  $\text{NO}_x$  species in the atmosphere, are shown in Fig. 4(b) and ESI

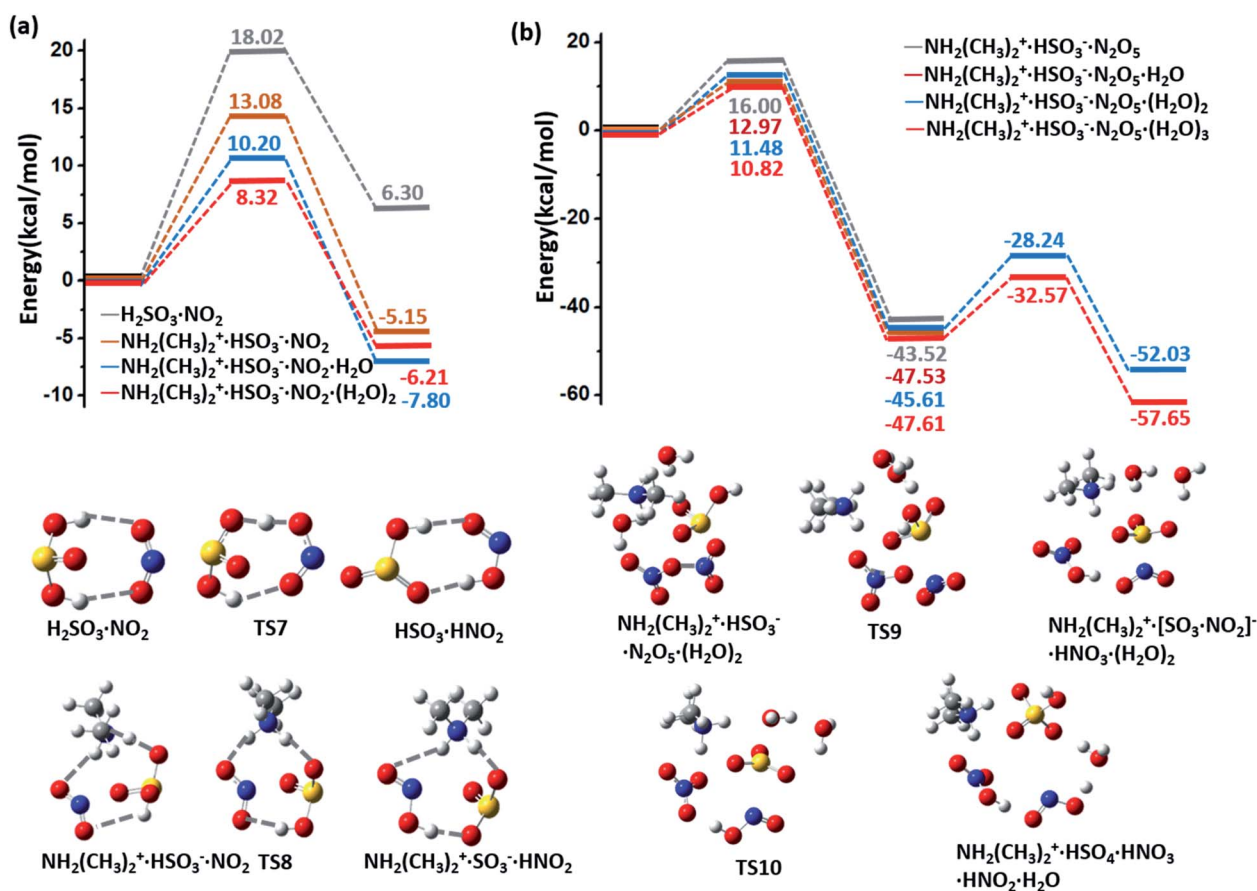


Fig. 4 (a) Potential energy profiles for the oxidation reactions of  $\text{H}_2\text{SO}_3/\text{CH}_2(\text{CH}_3)_2^+ \cdot \text{HSO}_3^- \cdot (\text{H}_2\text{O})_n$  and  $\text{NO}_2$  ( $n = 0-2$ ). (b) Potential energy profiles for the oxidation reaction for  $\text{H}_2\text{SO}_3/\text{NH}_2(\text{CH}_3)_2^+ \cdot \text{HSO}_3^- \cdot (\text{H}_2\text{O})_n$  ( $n = 0,1-3$ ) and  $\text{N}_2\text{O}_5$ . The energy profiles are calculated at the M06-2X/cc-pVDZ-F12 level with ZPE correction. Snapshots are taken from the BOMD simulation.



Table 1 Values of the total rate constants ( $k$ ,  $\text{cm}^3 \text{ molecule}^{-1} \text{ s}^{-1}$ ) for the hydrolysis reactions at temperatures from 240 to 300 K

Reaction	$k$ ( $\text{cm}^3 \text{ molecule}^{-1} \text{ s}^{-1}$ )			
	240 K	260 K	280 K	300 K
$\text{SO}_2 \cdot \text{H}_2\text{O} + \text{MA}$	$6.56 \times 10^{-13}$	$3.09 \times 10^{-13}$	$1.58 \times 10^{-13}$	$8.96 \times 10^{-14}$
$\text{SO}_2 \cdot \text{H}_2\text{O} + \text{DMA}$	$3.35 \times 10^{-10}$	$9.42 \times 10^{-11}$	$3.21 \times 10^{-11}$	$1.39 \times 10^{-11}$
$\text{SO}_2 \cdot (\text{H}_2\text{O})_2 + \text{MA}$	$3.79 \times 10^{-9}$	$3.17 \times 10^{-9}$	$1.18 \times 10^{-9}$	$4.22 \times 10^{-10}$
$\text{SO}_2 \cdot (\text{H}_2\text{O})_2 + \text{DMA}$	$9.01 \times 10^{-9}$	$7.26 \times 10^{-9}$	$5.64 \times 10^{-9}$	$4.53 \times 10^{-9}$

Fig. S6(c).<sup>†</sup> Similar to  $\text{O}_3$  oxidation, the process of  $(\text{NH}_2(\text{CH}_3)_2^+ \cdot \text{HSO}_3^- \cdot (\text{H}_2\text{O})_n + \text{N}_2\text{O}_5 \rightarrow \text{CH}_2(\text{CH}_3)_2^+ \cdot \text{HSO}_4^- \cdot (\text{H}_2\text{O})_{n-1} + \text{HNO}_3 + \text{HNO}_2)$  is a two-step reaction, where  $\text{N}_2\text{O}_5$  first dissociates into a  $\text{NO}_2^- \cdot \text{NO}_3^+$  ion pair and combines with the bisulfite cluster to form a  $\text{HNO}_3$  molecule and a stable complex  $[\text{SO}_3 \cdot \text{NO}_2]^-$  (Fig. 4(b)). The energy barrier of this step also decreases from 16.0 to 10.82  $\text{kcal mol}^{-1}$  as the number of participating water molecule increases ( $n = 0-3$ ). In the second step, a  $\text{H}_2\text{O}$  molecule that attacks the sulfur atom will assist the breaking of  $[\text{SO}_3 \cdot \text{NO}_2]^-$ , and the product  $\text{CH}_2(\text{CH}_3)_2^+ \cdot \text{HSO}_4^- \cdot \text{HNO}_3 \cdot \text{HNO}_2 \cdot (\text{H}_2\text{O})_{n-1}$  is finally formed. This step is also an exothermic process ( $\Delta E = -6.42$  and  $-10.04$   $\text{kcal mol}^{-1}$  for  $n = 2$  and  $3$ , respectively), and the barrier of this step is weakly affected by the number of water molecules ( $E_a = 17.37$  and  $15.04$   $\text{kcal mol}^{-1}$  for  $n = 2$  and  $3$ , respectively). Such high energy barriers indicate that  $\text{N}_2\text{O}_5$  plays a negligible role in the oxidation of sulfite.

#### 2.4 Kinetics and implications for atmospheric chemistry

The reaction rate constants of hydrolysis reactions are calculated based on TST, as listed in Table 1, and details of this calculation and the reactant concentrations are listed in ESI Tables S1, S2 and S3.<sup>†</sup> The rate constant for the hydrolysis reaction of  $\text{SO}_2 \cdot \text{H}_2\text{O}$  with DMA adopts an inverse relation with temperature, decreasing from  $3.35 \times 10^{-10}$  to  $1.39 \times 10^{-11}$   $\text{cm}^3 \text{ molecule}^{-1} \text{ s}^{-1}$  as the temperature changes from 240 to 300 K. According to previous observations,  $[\text{SO}_2]$  and  $[\text{DMA}]$  are  $\sim 10^{12}$

and  $\sim 10^9$   $\text{molecules cm}^{-3}$  in highly polluted air, respectively, while the concentration of  $\text{H}_2\text{O}$  decreases from  $9.7 \times 10^{17}$  to  $9.0 \times 10^{15}$   $\text{molecules cm}^{-3}$  at 100% relative humidity (RH) as the temperature drops from 300 K to 240 K.<sup>7,30,40</sup> On the basis of these parameters, the estimated concentrations of the  $\text{SO}_2 \cdot \text{H}_2\text{O}$  and  $\text{DMA} \cdot \text{H}_2\text{O}$  complexes at 300 K are approximately  $3.4 \times 10^8$  and  $1.9 \times 10^6$   $\text{molecules cm}^{-3}$ , respectively, and the rate of hydrolysis for  $\text{SO}_2$  and  $\text{H}_2\text{O}$  monomer assisted by DMA is estimated to be  $4.8 \times 10^6$   $\text{molecule cm}^{-3} \text{ s}^{-1}$ .

It is interesting to compare the rate of  $\text{SO}_2$  hydrolysis assisted by DMA to the rate of  $\text{SO}_2$  reacting with  $\text{OH} \cdot$  radicals under high RH conditions. The latter was previously thought to be the main reaction for  $\text{SO}_2$  oxidation. Using the average concentration of  $\text{OH} \cdot$  during the daytime ( $1 \times 10^6$   $\text{molecules cm}^{-3}$ ), the reaction rate of the oxidation of  $\text{SO}_2$  by  $\text{OH} \cdot$  based on a previously calculated rate constant ( $1.3 \times 10^{-12}$   $\text{cm}^3 \text{ molecule}^{-1} \text{ s}^{-1}$  at 300 K and 1 atm)<sup>41</sup> is  $1.5 \times 10^6$   $\text{molecule cm}^{-3} \text{ s}^{-1}$ , which is lower than the hydrolysis rate. In this case, the consumption of  $\text{SO}_2$  in the hydrolysis reaction can exceed that in the oxidation reaction with  $\text{OH} \cdot$  radicals. Similarly, the estimated hydrolysis rate for atmospheric  $\text{SO}_2$ , DMA, and  $(\text{H}_2\text{O})_2$  at 300 K and 100% RH is  $2.9 \times 10^6$   $\text{molecules per cm}^3$  per s, which is also more competitive with the reaction rate of  $\text{SO}_2$  and  $\text{OH} \cdot$ . Moreover, the concentration of  $\text{OH} \cdot$  would be further lowered due to the reduced photochemistry either during heavily polluted periods or at night time, when the hydrolysis reaction would even play an even more crucial role in  $\text{SO}_2$  oxidation.

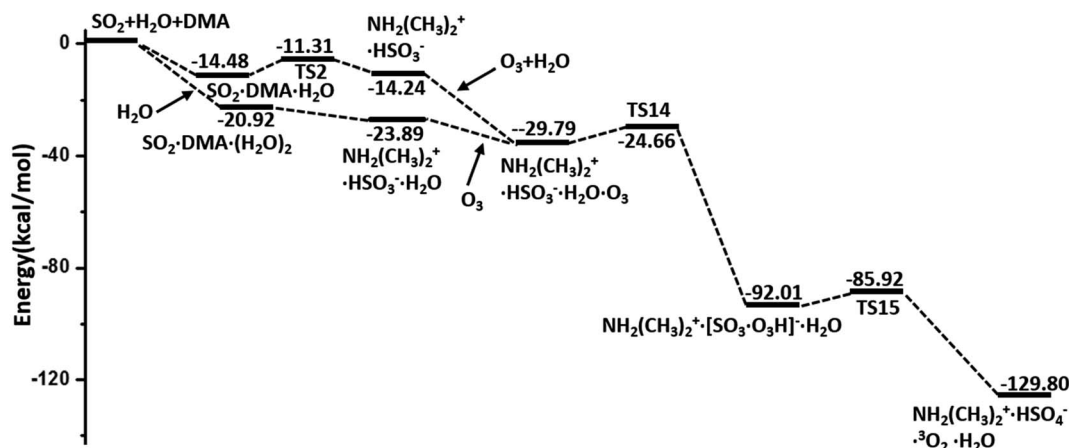


Fig. 5 Overall potential energy profiles for the hydrolysis of  $\text{SO}_2$  promoted by DMA and oxidized by  $\text{O}_3$  (M06-2X/cc-pVDZ-F12 with ZPE correction).



The hydration products  $\text{CH}_2(\text{CH}_3)_2^+ \cdot \text{HSO}_3^- \cdot (\text{H}_2\text{O})_n$  are expected to be oxidized by  $\text{O}_3$ ,  $\text{NO}_2$ , and  $\text{N}_2\text{O}_5$ . The estimated rate constant of the oxidation of  $\text{CH}_2(\text{CH}_3)_2^+ \cdot \text{HSO}_3^- \cdot (\text{H}_2\text{O})_2$  by  $\text{O}_3$  ( $5.82 \times 10^{-15} \text{ cm}^3 \text{ molecule}^{-1} \text{ s}^{-1}$ ) is 3 orders of magnitude higher than that of the oxidation by  $\text{NO}_2$  ( $1.73 \times 10^{-18} \text{ cm}^3 \text{ molecule}^{-1} \text{ s}^{-1}$ ). As the concentrations of  $\text{O}_3$ ,  $\text{NO}_2$  and  $\text{N}_2\text{O}_5$  were separately measured to be  $\sim 10^{12}$ ,  $\sim 10^{12}$ , and  $\sim 10^{10}$  molecules  $\text{cm}^{-3}$  in haze episodes, respectively,<sup>7,42</sup> we can estimate the lifetime of  $\text{CH}_2(\text{CH}_3)_2^+ \cdot \text{HSO}_3^- \cdot (\text{H}_2\text{O})_2$  by the expression  $\tau = (k \times [\text{oxidant}])^{-1}$ . The lifetime of  $\text{CH}_2(\text{CH}_3)_2^+ \cdot \text{HSO}_3^- \cdot (\text{H}_2\text{O})_2$  during oxidation by  $\text{O}_3$  is  $\sim 1/1000$  of that during oxidation by  $\text{NO}_2$  at 300 K. Considering the much lower oxidation rate constant and concentration of  $\text{N}_2\text{O}_5$  than  $\text{O}_3$  and  $\text{NO}_2$ , the oxidation by  $\text{N}_2\text{O}_5$  is negligible. As a result, the proposed hydrolysis of  $\text{SO}_2$  assisted by DMA in an  $\text{O}_3$ -polluted atmosphere is an important pathway for sulfate formation.

### 3 Conclusions

In summary, the hydrolysis and oxidation of  $\text{SO}_2$  promoted by DMA are studied by using QM calculations and BOMD simulations. In both gaseous and heterogeneous environments,  $\text{SO}_2$  can be easily hydrated with the assistance of DMA and then oxidized by  $\text{O}_3$ , as shown by the overall energy profile in Fig. 5. By contrast,  $\text{NO}_2$  and  $\text{N}_2\text{O}_5$ , also viewed as important oxidants in the atmosphere, appear to play a much less important role than  $\text{O}_3$  in the oxidation of  $\text{SO}_2$ . Kinetic analysis shows that the consumption rate of  $\text{SO}_2$  during hydrolysis in the presence of DMA can surpass the rate of oxidation with  $\text{OH}\cdot$  radicals under the conditions of heavily polluted air and high RH.

In the last decade,  $\text{O}_3$  levels in the global atmosphere, according to field measurements, have greatly increased. For example, it has been reported that the yearly mean concentration of  $\text{O}_3$  in Chinese megacities increased by 69% from 2006 to 2015.<sup>43</sup> The results from this research suggest that the hydrated oxidation of  $\text{SO}_2$  with amines and  $\text{O}_3$  has an important role in atmospheric chemistry.

### 4 Methods

#### 4.1 Details of QM calculations and BOMD simulations

The geometries of the reactant states, transition states, and product states in all the reactions are optimized at the unrestricted M06-2X/cc-pVDZ-F12 level,<sup>44–46</sup> which has shown good results on weak interactions and has been widely used in computational studies of atmospheric chemistry.<sup>16,46–48</sup> Zero-point energy (ZPE) corrections are included when calculating the potential energies, and intrinsic reaction coordinate (IRC) analysis is carried out to confirm the reaction pathways. WB97XD/cc-pVDZ-F12 and B2PLYPD/def2-TZVP methods are also employed for the total potential energy profiles for comparison, which show great consistency with energy profiles based on M06-2X. All the QM calculations for the reaction pathways are performed by using the Gaussian 09 software package.<sup>49</sup> The spin-polarized calculations are performed based on the generalized gradient approximation of the PBE functional, as implemented in the VASP 5.3.<sup>37,50–52</sup> A

kinetic energy cutoff of 400 eV is chosen for the plane-wave expansion. The cell size for the  $\text{NH}_2(\text{CH}_3)_2^+ \cdot [\text{SO}_3 \cdot \text{O}_3\text{H}]$  cluster is  $15 \times 15 \times 15 \text{ \AA}^3$ .

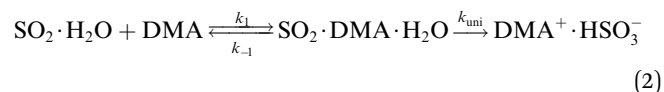
BOMD simulations are performed in the framework of the Becke–Lee–Yang–Parr (BLYP) functional<sup>53,54</sup> with the Quickstep module in CP2K code.<sup>55</sup> The Gaussian and plane wave (GPW) basis sets (280 Ry energy cutoff) combined with the Goedecker–Teter–Hutter (GTH) pseudopotential<sup>56</sup> are employed to obtain a good balance between computational cost and accuracy. In addition, the dispersion correction is also included to better describe weak intermolecular interactions.<sup>57</sup> Periodic boundary conditions are used, and the cell sizes for the  $\text{SO}_2 \cdot \text{MA}/\text{DMA} \cdot (\text{H}_2\text{O})_2$ ,  $\text{NH}_2(\text{CH}_3)_2^+ \cdot \text{HSO}_3^- \cdot \text{O}_3 \cdot (\text{H}_2\text{O})_4$ , and  $(\text{NH}_2(\text{CH}_3)_2^+)_2 \cdot \text{SO}_3^{2-} \cdot \text{O}_3 \cdot (\text{H}_2\text{O})_4$  systems are  $20 \times 20 \times 20 \text{ \AA}^3$ . A larger cell size ( $35 \times 35 \times 35 \text{ \AA}^3$ ) is chosen for the hydrolysis reaction of  $\text{SO}_2$  on the surface of a water nanodroplet containing 100 water molecules. The BOMD simulations are carried out at lower and higher temperatures (250 and 300 K), and the temperatures of the systems are controlled using the Nosé–Hoover thermostat. The time step of BOMD is set to 1.0 fs, which has been proven to achieve sufficient energy conservation for water systems.<sup>34,47,58</sup> The reaction process is unchanged with a smaller time step of 0.5 fs (ESI Fig. S7†).

#### 4.2 Calculation of the reaction rate constant

The rate constants of hydrolysis and oxidation reactions are evaluated using TST with Wigner tunnelling corrections.<sup>48,59,60</sup> As  $[\text{SO}_2][\text{DMA}]$  is negligible relative to  $[\text{SO}_2][\text{H}_2\text{O}]$  and  $[\text{DMA}][\text{H}_2\text{O}]$ , in the hydrolysis reaction of  $\text{SO}_2$  assisted by DMA, two reaction pathways are considered:  $\text{H}_2\text{O}$  first binding to  $\text{SO}_2$  and first binding to DMA. Because the concentrations of the reactants DMA,  $\text{SO}_2$ ,  $\text{SO}_2 \cdot \text{H}_2\text{O}$ , and  $\text{DMA} \cdot \text{H}_2\text{O}$  are critical to the final reaction rates, we estimate the number of  $\text{SO}_2 \cdot \text{H}_2\text{O}$  and  $\text{DMA} \cdot \text{H}_2\text{O}$  complexes by the following expressions:  $[\text{SO}_2 \cdot \text{H}_2\text{O}] = K_{\text{SO}_2 \cdot \text{H}_2\text{O}}[\text{SO}_2][\text{H}_2\text{O}]$  and  $[\text{DMA} \cdot \text{H}_2\text{O}] = K_{\text{DMA} \cdot \text{H}_2\text{O}}[\text{DMA}][\text{H}_2\text{O}]$ , where  $K_{\text{SO}_2 \cdot \text{H}_2\text{O}}$  and  $K_{\text{DMA} \cdot \text{H}_2\text{O}}$  are the equilibrium constants for the formation of  $\text{SO}_2 \cdot \text{H}_2\text{O}$  and  $\text{DMA} \cdot \text{H}_2\text{O}$  dimers, respectively. The total reaction rate  $\nu$  can be expressed as

$$\begin{aligned} \nu_{\text{SO}_2 \cdot \text{DMA} \cdot \text{H}_2\text{O}} &= k_{\text{SO}_2 \cdot \text{DMA} \cdot \text{H}_2\text{O}}[\text{SO}_2 \cdot \text{H}_2\text{O}][\text{DMA}] \\ &= k_{\text{SO}_2 \cdot \text{DMA} \cdot \text{H}_2\text{O}}[\text{SO}_2][\text{DMA} \cdot \text{H}_2\text{O}]. \end{aligned} \quad (1)$$

Taking the reaction of  $\text{SO}_2 \cdot \text{H}_2\text{O}$  and DMA as an example, the hydrolysis process is represented by



By assuming that the reactant complex  $\text{SO}_2 \cdot \text{DMA} \cdot \text{H}_2\text{O}$  is in equilibrium with the reactant monomers  $\text{SO}_2 \cdot \text{H}_2\text{O}$  and DMA, the total rate constant  $k_{\text{SO}_2 \cdot \text{DMA} \cdot \text{H}_2\text{O}}$  for the reaction can be written as

$$k_{\text{SO}_2 \cdot \text{DMA} \cdot \text{H}_2\text{O}} = \frac{k_1}{k_{-1}} k_{\text{uni}} = K_{\text{eq}} k_{\text{uni}} \quad (3)$$



where  $K_{\text{eq}}$  is the equilibrium constant for forming the reactant complex  $\text{SO}_2 \cdot \text{DMA} \cdot \text{H}_2\text{O}$  and is expressed by

$$K_{\text{eq}} = \exp\left(-\frac{\Delta G_{\text{eq}}}{RT}\right) \quad (4)$$

where  $\Delta G_{\text{eq}}$  is the free-energy change for the formation of the reactant complex,  $R$  is the gas constant, and  $T$  is the temperature. Here,  $k_{\text{uni}}$  is estimated by unimolecular TST and is expressed as

$$k_{\text{uni}} = \Gamma k_2 \quad (5)$$

The tunnelling effect factor  $\Gamma$  is given by Wigner tunnelling corrections,

$$\Gamma = 1 + \frac{1}{24} \left(\frac{h\nu^\ddagger}{k_B T}\right)^2 \quad (6)$$

where  $h$  is the Planck constant,  $\nu^\ddagger$  is the imaginary frequency of the transition state,  $k_B$  is the Boltzmann constant, and  $k_2$  is represented by

$$k_2 = \frac{k_B T}{h} \exp\left(-\frac{\Delta G}{RT}\right) \quad (7)$$

here,  $\Delta G$  is the activation free-energy change from the reactant complex to the transition state. The entropic term  $S$  is obtained from the partition function  $q(V, T)$  as

$$S = Nk_B + Nk_B \ln\left(\frac{q(V, T)}{N}\right) + Nk_B T \left(\frac{\partial q(V, T)}{\partial T}\right)_V \quad (8)$$

where  $q(V, T)$  is determined from the calculation of vibrational frequency.

## Conflicts of interest

There are no conflicts to declare.

## Acknowledgements

We thank Dr Jinrong Yang for valuable discussions. HL is thankful for the funding support from the National Natural Science Foundation of China (21773005). JSF and X CZ acknowledge computer support from UNL Holland Computing Center.

## Notes and references

- 1 F. Bianchi, J. Trostl, H. Junninen, C. Frege, S. Henne, C. R. Hoyle, U. Molteni, E. Herrmann, A. Adamov, N. Bukowiecki, X. Chen, J. Duplissy, M. Gysel, M. Hutterli, J. Kangasluoma, J. Kontkanen, A. Kurten, H. E. Manninen, S. Munch, O. Perakyla, T. Petaja, L. Rondo, C. Williamson, E. Weingartner, J. Curtius, D. R. Worsnop, M. Kulmala, J. Dommen and U. Baltensperger, *Science*, 2016, **352**, 1109–1112.
- 2 M. Kulmala, J. Kontkanen, H. Junninen, K. Lehtipalo, H. E. Manninen, T. Nieminen, T. Petaja, M. Sipila, S. Schobesberger, P. Rantala, A. Franchin, T. Jokinen, E. Jarvinen, M. Aijala, J. Kangasluoma, J. Hakala, P. P. Aalto, P. Paasonen, J. Mikkila, J. Vanhanen, J. Aalto, H. Hakola, U. Makkonen, T. Ruuskanen, R. L. Mauldin 3rd, J. Duplissy, H. Vehkamaki, J. Back, A. Kortelainen, I. Riipinen, T. Kurten, M. V. Johnston, J. N. Smith, M. Ehn, T. F. Mentel, K. E. Lehtinen, A. Laaksonen, V. M. Kerminen and D. R. Worsnop, *Science*, 2013, **339**, 943–946.
- 3 A. Kurten, F. Bianchi, J. Almeida, O. Kupiainen-Määttä, E. M. Dunne, J. Duplissy, C. Williamson, P. Barmet, M. Breitenlechner, J. Dommen, N. M. Donahue, R. C. Flagan, A. Franchin, H. Gordon, J. Hakala, A. Hansel, M. Heinritzi, L. Ickes, T. Jokinen, J. Kangasluoma, J. Kim, J. Kirkby, A. Kupc, K. Lehtipalo, M. Leiminger, V. Makhmutov, A. Onnela, I. K. Ortega, T. Petäjä, A. P. Praplan, F. Riccobono, M. P. Rissanen, L. Rondo, R. Schnitzhofer, S. Schobesberger, J. N. Smith, G. Steiner, Y. Stozhkov, A. Tomé, J. Tröstl, G. Tsagkogeorgas, P. E. Wagner, D. Wimmer, P. Ye, U. Baltensperger, K. Carslaw, M. Kulmala and J. Curtius, *J. Geophys. Res.: Atmos.*, 2016, **121**, 12377–12400.
- 4 R. Zhang, A. Khalizov, L. Wang, M. Hu and W. Xu, *Chem. Rev.*, 2012, **112**, 1957–2011.
- 5 Y. Cheng, G. Zheng, C. Wei, Q. Mu, B. Zheng, Z. Wang, M. Gao, Q. Zhang, K. He, G. Carmichael, U. Pöschl and H. Su, *Sci. Adv.*, 2016, **2016**, e1601530.
- 6 D. L. Yue, M. Hu, R. Y. Zhang, Z. B. Wang, J. Zheng, Z. J. Wu, A. Wiedensohler, L. Y. He, X. F. Huang and T. Zhu, *Atmos. Chem. Phys.*, 2010, **10**, 4953–4960.
- 7 G. J. Zheng, F. K. Duan, H. Su2, Y. L. Ma, Y. Cheng, B. Zheng, Q. Zhang, T. Huang, T. Kimoto, D. Chang, U. Pöschl, Y. F. Cheng and K. B. He, *Atmos. Chem. Phys.*, 2015, **2015**, 2969–2983.
- 8 J. Almeida, S. Schobesberger, A. Kurten, I. K. Ortega, O. Kupiainen-Maatta, A. P. Praplan, A. Adamov, A. Amorim, F. Bianchi, M. Breitenlechner, A. David, J. Dommen, N. M. Donahue, A. Downard, E. Dunne, J. Duplissy, S. Ehrhart, R. C. Flagan, A. Franchin, R. Guida, J. Hakala, A. Hansel, M. Heinritzi, H. Henschel, T. Jokinen, H. Junninen, M. Kajos, J. Kangasluoma, H. Keskinen, A. Kupc, T. Kurten, A. N. Kvashin, A. Laaksonen, K. Lehtipalo, M. Leiminger, J. Leppa, V. Loukonen, V. Makhmutov, S. Mathot, M. J. McGrath, T. Nieminen, T. Olenius, A. Onnela, T. Petaja, F. Riccobono, I. Riipinen, M. Rissanen, L. Rondo, T. Ruuskanen, F. D. Santos, N. Sarnela, S. Schallhart, R. Schnitzhofer, J. H. Seinfeld, M. Simon, M. Sipila, Y. Stozhkov, F. Stratmann, A. Tome, J. Trostl, G. Tsagkogeorgas, P. Vaattovaara, Y. Viisanen, A. Virtanen, A. Vrtala, P. E. Wagner, E. Weingartner, H. Wex, C. Williamson, D. Wimmer, P. Ye, T. Yli-Juuti, K. S. Carslaw, M. Kulmala, J. Curtius, U. Baltensperger, D. R. Worsnop, H. Vehkamaki and J. Kirkby, *Nature*, 2013, **502**, 359–363.
- 9 D. R. Hanson, *J. Geophys. Res.*, 2002, **107**, 4158.
- 10 W.-K. Li and M. L. McKee, *J. Phys. Chem. A*, 1997, **101**, 9778–9782.
- 11 J. J. Margitan, *J. Phys. Chem. A*, 1984, **88**, 3314–3318.



- 12 P. H. Wine, R. J. Thompson, A. R. Ravishankara, D. H. Semmes, C. A. Gump, A. Torabi and J. M. Nicovich, *J. Phys. Chem.*, 1983, **88**, 2095–2104.
- 13 R. L. Mauldin, T. Berndt, M. Sipila, P. Paasonen, T. Petaja, S. Kim, T. Kurten, F. Stratmann, V. M. Kerminen and M. Kulmala, *Nature*, 2012, **488**, 193–196.
- 14 Z. Chen, C. Liu, W. Liu, T. Zhang and J. Xu, *Sci. Total Environ.*, 2017, **575**, 429–436.
- 15 F. Sheng, L. Jingjing, C. Yu, T. Fu-Ming, D. Xuemei and L. Jing-yao, *RSC Adv.*, 2018, **8**, 7988–7996.
- 16 H. Zhang, S. Chen, J. Zhong, S. Zhang, Y. Zhang, X. Zhang, Z. Li and X. C. Zeng, *Atmos. Environ.*, 2018, **177**, 93–99.
- 17 J. Yang, L. Li, S. Wang, H. Li, J. S. Francisco, X. C. Zeng and Y. Gao, *J. Am. Chem. Soc.*, 2019, **141**, 19312–19320.
- 18 R. Steudel and Y. Steudel, *Eur. J. Inorg. Chem.*, 2009, **2009**, 1393–1405.
- 19 T. Loerting and K. R. Liedl, *J. Phys. Chem. A*, 2001, **105**, 5137–5145.
- 20 A. F. Voegelé, C. S. Tautermann, C. Rauch, T. Loerting and K. R. Liedl, *J. Phys. Chem. A*, 2004, **108**, 3859–3864.
- 21 J. Kirkby, J. Curtius, J. Almeida, E. Dunne, J. Duplissy, S. Ehrhart, A. Franchin, S. Gagne, L. Ickes, A. Kurten, A. Kupc, A. Metzger, F. Riccobono, L. Rondo, S. Schobesberger, G. Tsagkogeorgas, D. Wimmer, A. Amorim, F. Bianchi, M. Breitenlechner, A. David, J. Dommen, A. Downard, M. Ehn, R. C. Flagan, S. Haider, A. Hansel, D. Hauser, W. Jud, H. Junninen, F. Kreissl, A. Kvashin, A. Laaksonen, K. Lehtipalo, J. Lima, E. R. Lovejoy, V. Makhmutov, S. Mathot, J. Mikkila, P. Minginette, S. Mogo, T. Nieminen, A. Onnela, P. Pereira, T. Petaja, R. Schnitzhofer, J. H. Seinfeld, M. Sipila, Y. Stozhkov, F. Stratmann, A. Tome, J. Vanhanen, Y. Viisanen, A. Vrtala, P. E. Wagner, H. Walther, E. Weingartner, H. Wex, P. M. Winkler, K. S. Carslaw, D. R. Worsnop, U. Baltensperger and M. Kulmala, *Nature*, 2011, **476**, 429–433.
- 22 J. Liu, S. Fang, W. Liu, M. Wang, F. M. Tao and J. Y. Liu, *J. Phys. Chem. A*, 2015, **119**, 102–111.
- 23 Y. You, V. P. Kanawade, J. A. de Gouw, A. B. Guenther, S. Madronich, M. R. Sierra-Hernández, M. Lawler, J. N. Smith, S. Takahama, G. Ruggeri, A. Koss, K. Olson, K. Baumann, R. J. Weber, A. Nenes, H. Guo, E. S. Edgerton, L. Porcelli, W. H. Brune, A. H. Goldstein and S. H. Lee, *Atmos. Chem. Phys.*, 2014, **14**, 12181–12194.
- 24 J. Zheng, Y. Ma, M. Chen, Q. Zhang, L. Wang, A. F. Khalizov, L. Yao, Z. Wang, X. Wang and L. Chen, *Atmos. Environ.*, 2015, **102**, 249–259.
- 25 M. Chen, M. Titcombe, J. Jiang, C. Jen, C. Kuang, M. L. Fischer, F. L. Eisele, J. I. Siepmann, D. R. Hanson, J. Zhao and P. H. McMurry, *Proc. Natl. Acad. Sci. U. S. A.*, 2012, **109**, 18713–18718.
- 26 C. Qiu, L. Wang, V. Lal, A. F. Khalizov and R. Zhang, *Environ. Sci. Technol.*, 2011, **45**, 4748–4755.
- 27 S. M. Murphy, A. Sorooshian, J. H. Kroll, N. L. Ng, P. Chhabra, C. Tong, J. D. Surratt, E. Knipping, R. C. Flagan and J. H. Seinfeld, *Atmos. Chem. Phys.*, 2007, **7**, 289–349.
- 28 H. Yu, R. McGraw and S.-H. Lee, *Geophys. Res. Lett.*, 2012, **39**, L02807.
- 29 C. Qiu and R. Zhang, *Phys. Chem. Chem. Phys.*, 2013, **15**, 5738–5752.
- 30 L. Yao, O. Garmash, F. Bianchi, J. Zheng, C. Yan., J. Kontkanen, H. Junninen, S. B. Mazon, M. Ehn, P. Paasonen, M. Sipilä, M. Wang, X. Wang, S. Xiao, H. Chen, Y. Lu, B. Zhang, D. Wang, Q. Fu, F. Geng, L. Li, H. Wang, L. Qiao, X. Yang, J. Chen, V.-M. Kerminen, T. Petäjä, D. R. Worsnop, M. Kulmala and L. Wang, *Science*, 2018, **361**, 278–281.
- 31 H. Li, J. Zhong, H. Vehkamäki, T. Kurten, W. Wang, M. Ge, S. Zhang, Z. Li, X. Zhang, J. S. Francisco and X. C. Zeng, *J. Am. Chem. Soc.*, 2018, **140**, 11020–11028.
- 32 B. J. Finlayson-Pitts, L. M. Wingen, A. L. Sumner, D. Syomin and K. A. Ramazan, *Phys. Chem. Chem. Phys.*, 2003, **5**, 223–242.
- 33 Y. Miller., B. J. Finlayson-Pitts and R. B. Gerber, *J. Am. Chem. Soc.*, 2009, **131**, 12180–12185.
- 34 J. Zhong, C. Zhu, L. Li, G. L. Richmond, J. S. Francisco and X. C. Zeng, *J. Am. Chem. Soc.*, 2017, **139**, 17168–17174.
- 35 C. Schweitzer and R. Schmid, *Chem. Rev.*, 2003, **103**, 1685–1757.
- 36 J. P. Perdew, K. Burke and M. Ernzerhof, *Phys. Rev. Lett.*, 1996, **77**, 3865–3868.
- 37 J. Furthmüller, J. Hafner and G. Kresse, *Phys. Rev. B: Condens. Matter Mater. Phys.*, 1994, **50**, 15606–15622.
- 38 A. J. M. Anglada, S. Olivella and A. Solé, *Phys. Chem. Chem. Phys.*, 2014, **16**, 19437–19445.
- 39 C. Ye, N. Zhang, H. Gao and X. Zhou, *Environ. Sci. Technol.*, 2017, **51**, 6849–6856.
- 40 M. E. Dunn, E. K. Pokon and G. C. Shields, *J. Am. Chem. Soc.*, 2003, **126**, 2647–2653.
- 41 B. Long, J. L. Bao and D. G. Truhlar, *Phys. Chem. Chem. Phys.*, 2017, **19**, 8091–8100.
- 42 H. Wang, K. Lu, X. Chen, Q. Zhu, Q. Chen, S. Guo, M. Jiang, X. Li, D. Shang, Z. Tan, Y. Wu, Z. Wu, Q. Zou, Y. Zheng, L. Zeng, T. Zhu, M. Hu and Y. Zhang, *Environ. Sci. Technol.*, 2017, **4**, 416–420.
- 43 W. Gao, X. Tie, J. Xu, R. Huang, X. Mao, G. Zhou and L. Chang, *Sci. Total Environ.*, 2017, **603–604**, 425–433.
- 44 C. Hattig, W. Klopffer, A. Kohn and D. P. Tew, *Chem. Rev.*, 2012, **112**, 4–74.
- 45 G. Knizia, T. B. Adler and H. J. Werner, *J. Chem. Phys.*, 2009, **130**, 054104.
- 46 Y. Zhao and D. G. Truhlar, *Theor. Chem. Acc.*, 2008, **120**, 215–241.
- 47 J. Zhong, H. Li, M. Kumar, J. Liu, L. Liu, X. Zhang, X. C. Zeng and J. S. Francisco, *Angew. Chem., Int. Ed. Engl.*, 2019, **58**, 8351–8355.
- 48 R. Wu, S. Pan, Y. Li and L. Wang, *J. Phys. Chem. A*, 2014, **118**, 4533–4547.
- 49 M. J. Frisch, G. W. Trucks, H. B. Schlegel, G. E. Scuseria, M. A. Robb, J. R. Cheeseman, G. Scalmani, V. Barone, G. A. Petersson, H. Nakatsuji, X. Li, M. Caricato, A. Marenich, J. Bloino, B. G. Janesko, R. Gomperts, B. Mennucci, H. P. Hratchian, J. V. Ortiz, A. F. Izmaylov,



- J. L. Sonnenberg, D. Williams-Young, F. Ding, F. Lipparini, F. Egidi, J. Goings, B. Peng, A. Petrone, T. Henderson, D. Ranasinghe, V. G. Zakrzewski, J. Gao, N. Rega, G. Zheng, W. Liang, M. Hada, M. Ehara, K. Toyota, R. Fukuda, J. Hasegawa, M. Ishida, T. Nakajima, Y. Honda, O. Kitao, H. Nakai, T. Vreven, K. Throssell, J. A. Montgomery Jr, J. E. Peralta, F. Ogliaro, M. Bearpark, J. J. Heyd, E. Brothers, K. N. Kudin, V. Staroverov, T. N. Keith, R. Kobayashi, J. Normand, K. Raghavachari, A. Rendell, J. C. Burant, S. S. Iyengar, J. Tomasi, M. Cossi, J. M. Millam, M. Klene, C. Adamo, R. Cammi, J. W. Ochterski, R. L. Martin, K. Morokuma, O. Farkas, J. B. Foresman and D. J. Fox, *Gaussian 09, Revision D.01*, Gaussian Inc., Wallingford, CT, 2009.
- 50 G. Kresse and J. Hafner, *Phys. Rev. B: Condens. Matter Mater. Phys.*, 1993, **47**, 558.
- 51 G. Kresse and J. Furthmüller, *Comput. Mater. Sci.*, 1996, **6**, 15–50.
- 52 G. Kresse and J. Furthmüller, *Phys. Rev. B: Condens. Matter Mater. Phys.*, 1996, **54**, 11169–11186.
- 53 A. D. Becke, *Phys. Rev. A: At., Mol., Opt. Phys.*, 1988, **38**, 3098.
- 54 C. Lee, W. Yang and R. G. Parr, *Phys. Rev. B: Condens. Matter Mater. Phys.*, 1988, **37**, 785–789.
- 55 J. VandeVondele, F. Mohamed, M. Krack, J. Hutter, M. Sprik and M. Parrinello, *J. Chem. Phys.*, 2005, **122**, 14515.
- 56 G. Lippert, J. Hutter and M. Parrinello, *Mol. Phys.*, 2010, **92**, 477–488.
- 57 S. Grimme, J. Antony, S. Ehrlich and H. Krieg, *J. Chem. Phys.*, 2010, **132**, 154104.
- 58 C. Zhu, M. Kumar, J. Zhong, L. Li, J. S. Francisco and X. C. Zeng, *J. Am. Chem. Soc.*, 2016, **138**, 11164–11169.
- 59 J. Elm, S. Jorgensen, M. Bilde and K. V. Mikkelsen, *Phys. Chem. Chem. Phys.*, 2013, **15**, 9636–9645.
- 60 H. S. Johnston and J. Heicklen, *J. Chem. Phys.*, 1962, **66**, 532–533.

